Thin Solid Films 773 (2023) 139825

Contents lists available at ScienceDirect

Thin Solid Films

journal homepage: www.elsevier.com/locate/tsf

Anomalous optical properties of bismuth ultrathin film using spectroscopic ellipsometry in the visible - Ultraviolet range

Ruth Meisye Kaloari [a], Eri Widianto [a,b], I Ketut Agus Putra Dana [a], Arif Lukmantoro [a], Edi Suharyadi [a], Takeshi Kato [c], Satoshi Iwata [c], Moh . Adhib Ulil Absor [a], Iman Santoso [a,*]

[a] Department of Physics, Faculty of Mathematics and Natural Sciences, Universitas Gadjah Mada, Sekip Utara PO Box BLS 21, Yogyakarta 55281, Indonesia
[b] Department of Mechanical Engineering, Faculty of Engineering, Universitas Singaperbangsa Karawang, Telukjambe Timur, Karawang 41361, Indonesia
[c] Institute of Materials and Systems for Sustainability, Nagoya University, Nagoya, Japan

ARTICLE INFO

Keywords:
Optical properties
Bismuth
Spectroscopic ellipsometry
Quantum confinement effect

ABSTRACT

We report the study of optical properties of Bismuth (Bi) thin films with different thicknesses (t_{Bi} = 25 nm, 20 nm, 15 nm, and 5 nm) using spectroscopic ellipsometry in the visible – ultraviolet light range (1.4 – 5.3 eV). A broad absorption hump and three broad absorption peaks, as represented by the imaginary part of the dielectric constant and real part of optical conductivity, occur at 2.0 eV and 2.8 eV; 3.8 eV, and 5.0 eV, respectively, for t_{Bi} of 25 nm, 20 nm, and 15 nm. The absorption features might be related to electron transition involving p_x, p_y orbitals to p_z orbital throughout the high symmetry line of Bi's first Brillouin zone. These absorption peaks decreased as t_{Bi} decreased from 25 nm to 15 nm. However, a significant increase in those absorption peaks when t_{Bi} = 5 nm accompanied by extra absorption peaks at 2.6 eV, 3.0 eV, and 4.1 eV. This anomalous is possibly due to the transition from three-dimension to two-dimension by the quantum confinement effect, leading to the increase of density of state as the Bi goes to ultrathin-film thickness. We did the first principle calculation (density functional theory) based on bulk Bi and Bi thin film to support this observation. By using more precise optical properties of this material, our study may provide insight into the future development of Bi-enabled technologies.

1. Introduction

Bismuth (Bi) is a material that has excellent electronic and optical properties due to its unique electronic band structure, low carrier effective mass, and low carrier density [1–9]. The lower effective masses of the charge carriers at the Fermi level cause confinement effects, which may enhance the energy difference between the valence and conduction bands [10–12] and many researchers have predicted and investigated a semimetal-to-semiconductor transition in the nanoscale thickness domain [13,14]. Even though the transition to the semiconducting phase provides considerable application potential, it is still a topic of robust debate. Consideration must be given to the increased significance of surface states as the surface-to-volume ratio increases in very thin films. Many possible uses exist in the current industry, including superconductivity, giant magnetoresistance, thermoelectric, optoelectronic devices, photocatalytic, and batteries [15–23]. Bi nanostructures allow for the exploration and manipulation of material properties, making them attractive from both a physics and an application aspect.

In bulk Bi, a weak overlap between valence and conduction bands yields the formation of free electrons and holes pocket in the vicinity of the Fermi level. The free electrons lie in the electron pocket at *L* point of Bi Brillouin zone and have a linear dispersion with a very small effective mass. Meanwhile, the holes reside in the hole pocket at *A* point of Bi Brillouin zone, and it has, on the contrary, a large effective mass [24–26]. This peculiar electronic band structure yields to the semi metallicity leading to exceptional features such as the observation of a large diamagnetism [27], high Seebeck thermoelectric coefficient [28], Hall effect [27,28], and even superconductivity [17,21]. On the other hand, Bi in the form of nanostructures sparked a broad interest recently [1,2]. Bi has been recognized as an essential component in two-dimensional topological insulators. Indeed, at their ultrathin conditions, Bi films were theoretically projected to be two-dimensional topological insulators [27,29]. Due to the very large Fermi wavelength (λ_F = 20 − 30 nm), the quantum confinement manifested in the

* Corresponding author. Department of Physics, Faculty of Mathematics and Natural Sciences, Universitas Gadjah Mada, Sekip Utara PO Box BLS 21, Yogyakarta 55281, Indonesia.
E-mail address: iman.santoso@ugm.ac.id (I. Santoso).

https://doi.org/10.1016/j.tsf.2023.139825
Received 14 November 2022; Received in revised form 3 April 2023; Accepted 4 April 2023
Available online 6 April 2023

thickness of tens of nanometers for thin films or nanowires. Ishida demonstrated, in particular, that the surface states at the Γ and *M* points extend significantly into the core of the film [30]. As a result, the effect of quantum confinement is most apparent in these regions. The surface states of the films are also crucial in understanding the topological features of Bi and their development in two-dimensional films impacted by quantum confinement [31]. Moreover, since Bi is a heavy element, then very strong spin-orbit coupling (SOC) could be present. The interplay between SOC and several symmetries in the Bi crystalline leads to the observation of Rashba splitting and the topologically protected surface state of their band structure in the vicinity of the Fermi level, which is very important for application in spintronics and quantum computing [10,11,32,33].

Optical spectroscopy has been used to reveal the electronic structure of both Bi bulk and film [6,8,34–37]. The optical properties of bulk Bi are characterized by the presence of giant infrared absorption [38], plasmarons due to many-body effects at very low energy [39], and strong absorption in the visible – ultraviolet range [38,40]. Meanwhile, the Bi films provide almost similar optical properties as bulk Bi [40,6]. A recent optical study of Bi thin films in infrared to ultraviolet (0.05 eV to 4 eV) with the thickness varied from 78 nm down to 17 nm done by Toudert et al. reveals that the dielectric function of the film possesses similar optical features to that of bulk. For the thickness of 11 nm, the dielectric function slightly deviated from that of bulk Bi, which might be caused by the effective mix between Bi and air rather than the quantum confinement effect, although the Bi layer has a discontinuous structure [6]. However, the quantum confinement effect could manifest in a Bi thin film that has a discontinuous structure for a thickness of less than 11 nm [32]. If the quantum confinement effect is not present, then the absorption should decrease monotonically as the thickness decreases. Therefore it is crucial to study the role of quantum confinement in the optical properties of Bi films for very thin thickness (less than 11 nm) and broader optical range to provide us with a better understanding of the electronic structure of Bi films. Understanding the dielectric function of Bi nanostructures across a wide spectral range is required to fully realize the promise of such applications via reasonable nanostructure design. Because the performances of these films are significantly dependent on their thicknesses and dielectric functions, properly describing these characteristics of such Bi thin films for improved applications is very important.

Here, we study the evolution of complex dielectric constant and optical conductivity of ultrathin Bi film with the thickness varied from $t_{Bi} = 25$ nm to $t_{Bi} = 5$ nm using spectroscopy ellipsometry in the optical range of 1.4 eV to 5.3 eV. Bi thin films of different thicknesses were deposited on Al_2O_3 substrate by radio frequency (RF) magnetron sputtering. In addition, we furthermore discuss the electronic states of Bi near the Fermi level as calculated with density functional theory (DFT). This study may offer some insight into the future development of Bi-enabled technology by using more precise optical properties of this material.

2. Experimental details

2.1. Sample preparation

High-purity Bismuth (Bi metal 4 N target, ∅ 101.6 × *t* 5, 99.99%) and alumina (Al_2O_3 4 N target, ∅ 101.6 × *t* 5, 99.99%) were purchased from Kojundo Chemical Laboratory Co., Ltd., Japan. The Bi thin films were fabricated by RF magnetron sputtering on the Al_2O_3 with a thickness of 200 nm that is coated on a glass substrate (25.4 × 76.2 mm) at room temperature. Prior to deposition, the glass substrate was sequentially cleaned with isopropanol, acetone, ethanol, and deionized (DI) water. During the process of depositing the film, the power used for RF sputtering was 40 W, and the Argon gas pressure was maintained at 4 Pa. The substrate temperature was kept at 100 °C, and the target-substrate distance was fixed at 10 cm for all films. All films were deposited for 30 min to produce films of Al_2O_3 and Bi with a thickness of several hundred nanometers, approximately 167 nm, which is determined using a KLA Tencor Alpha-Step IQ Profilometer, yielding to the deposition rate of 0.093 nm/s. The Bi deposition time was adjusted based on the Bi deposition rate to obtain films with nominal thicknesses, ranging from 5 nm to 25 nm. As for Al_2O_3, the deposition time was adjusted based on the same deposition rate to obtain the Al_2O_3 film with nominal thickness of 200 nm. The thickness of film was determined directly during fabrication by adjusting the sputtering time of the films by the following empirical equation: $t = \frac{d}{v}$, where *t*, *d*, and *v* are the sputtering deposition time, the thickness of the Bi thin film, and the sputtering deposition rate, respectively, similar to that described previously [35,41,42]. The deposition parameters for preparing the films are shown in Table 1.

A scanning electron microscope SEM (JSM-IT200 operating at 20 kV) was used to characterize the cross-section topography. The surface morphology and roughness were investigated using atomic force microscopy AFM (Park Systems).

2.2. Spectroscopic ellipsometry measurements

The spectroscopic ellipsometry (SE) measurements were carried out with homemade rotating analyzer ellipsometry (RAE) in the photon energy range of 1.4 – 5.3 eV, as described in previous works [43–45]. The measurement was performed at an incident angle (θ_0) of 70°, and the polarizer angle was fixed at 45°. The optical constants of Bi thin film were extracted using the 5-layer optical Fresnel model given in Fig. 1. The model consists of air/EMA/Bi/alumina/glass in which we include the Bruggeman effective medium approximation (EMA) layer that constitutes mixed between the fraction of air and fraction of Bi film. The relation between the SE parameters (ψ and Δ) and the optical constant is given by [46,47]:

$$\rho \equiv \tan(\psi)\exp(i\Delta) \equiv, \frac{r_{,01,234,p},}{r_{,01,234,s}} \tag{1}$$

The $r_{,01,234,p}(r_{,01,234,s})$ represents the reflectivity coefficient of *p*(*s*) polarized light of our 5-layer optical model, which is given by:

$$r_{,012,34} = \frac{r_{01} + r_{1234}\exp(-i2\beta_1)}{1 + r_{01}r_{1234}\exp(-i2\beta_1)} \tag{2.a}$$

$$r_{1234} = \frac{r_{12} + (r_{23} + r_{34}\exp(-i2\beta_3))\exp(-i2\beta_2)}{1 + r_{12}(1 + r_{23}r_{34}\exp(-i2\beta_3))\exp(-i2\beta_2)} \tag{2.b}$$

where, $\beta_1 = (2\pi d_1\sqrt{\varepsilon_1 - \varepsilon_0\sin^2\theta_0})/\lambda$, $\beta_2 = (2\pi d_2\sqrt{\varepsilon_2 - \varepsilon_0\sin^2\theta_0})/\lambda$, and $\beta_3 = (2\pi d_3\sqrt{\varepsilon_3 - \varepsilon_0\sin^2\theta_0})/\lambda$. The d_1, d_2, and d_3 are the thickness of the EMA layer, Bi layer, and alumina layer; meanwhile, the ε_1, ε_2, and ε_3 denote their complex dielectric constant, respectively.

The reflectivity coefficient of the consecutive layer can be calculated using the Fresnel equation [46,47]:

$$r_{mn,p} = \frac{\sqrt{\frac{\varepsilon_n}{\varepsilon_m}}(\varepsilon_m - \varepsilon_0\sin^2\theta_0)^{\frac{1}{2}} - \sqrt{\frac{\varepsilon_m}{\varepsilon_n}}(\varepsilon_n - \varepsilon_0\sin^2\theta_0)^{\frac{1}{2}}}{\sqrt{\frac{\varepsilon_n}{\varepsilon_m}}(\varepsilon_m - \varepsilon_0\sin^2\theta_0)^{\frac{1}{2}} + \sqrt{\frac{\varepsilon_m}{\varepsilon_n}}(\varepsilon_n - \varepsilon_0\sin^2\theta_0)^{\frac{1}{2}}} \tag{3.a}$$

Table 1
List of conditions for preparing Bi and Al_2O_3 films by RF sputtering.

Sample	Deposition time *t* (s)	Deposition rate *v* (nm/s)	Thickness *d* (nm)
$t_{Bi} = 25$ nm	269	0.093	25
$t_{Bi} = 20$ nm	216	0.093	20
$t_{Bi} = 15$ nm	162	0.093	15
$t_{Bi} = 5$ nm	54	0.093	5
Al_2O_3	2151	0.093	200

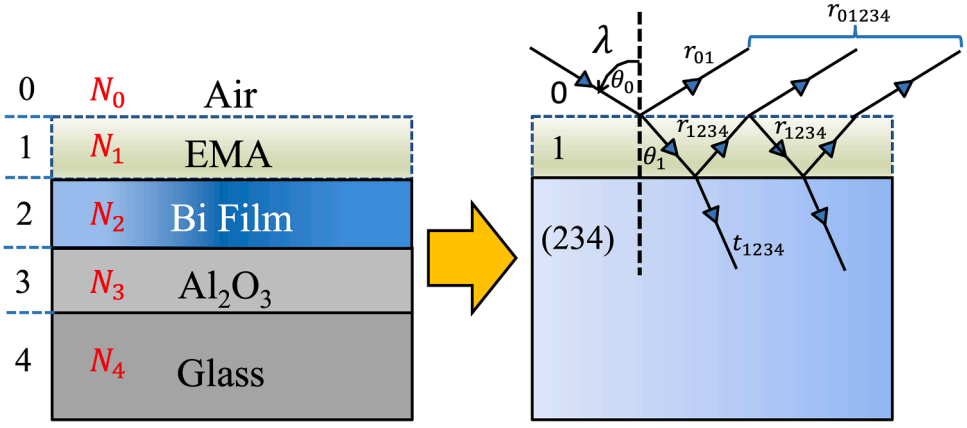

Fig. 1. The optical calculation model based on a 5-layer Fresnel equation is used in this work.

$$r_{mn,s} = \frac{(\varepsilon_m - \varepsilon_0 \sin^2\theta_0)^{\frac{1}{2}} - (\varepsilon_n - \varepsilon_0 \sin^2\theta_0)^{\frac{1}{2}}}{(\varepsilon_m - \varepsilon_0 \sin^2\theta_0)^{\frac{1}{2}} + (\varepsilon_n - \varepsilon_0 \sin^2\theta_0)^{\frac{1}{2}}} \tag{3.b}$$

where m and n represent the consecutive index. The fitting procedure was conducted by best matching ψ and Δ data from the experiment with Cauchy, Drude-Lorentz, and the Bruggeman EMA model. The Cauchy model was used for transparent material that we used in this study, i.e., alumina and glass, which is given by:

$$N = A + \frac{B}{\lambda^2} + \frac{C}{\lambda^4} + \ldots; k = 0 \tag{4}$$

where A, B, and C are fitting constants. The fitting result of the bulk glass and Al_2O_3 films using Cauchy models is tabulated in Table 2. These parameters were constant for each thickness, while only the Drude-Lorentz parameters were adjusted.

The free parameters used were the transfer frequency, which is related to the peak position (ω_0), the oscillator peak, which is related to the plasma frequency (ω_p), the width of the oscillator (Γ), the thickness of Bi layer (d_2), and the thickness of the alumina substrate (d_3). Furthermore, the Drude-Lorentz model was used for metallic materials in this study to model the Bi layer. In contrast, the Bruggeman EMA theory was used to model the mix between air and Bi layer. The Bruggeman EMA seems to be caused by the roughness and morphology of a thin layer of Bi that is uneven to form an island [35,6].

By measuring Ψ and Δ, the optical constants of the samples can be calculated. However, this is not a simplistic procedure since the sample must be modelled, and the data produced by the model should be compared to the experimental result while adjusting the parameters, such as optical constants and film thickness. The value that closely matches the experimental data is determined during this iteration procedure by reducing the mean square error (χ^2) [46]:

$$\chi^2 = \chi^2_{\text{psi}} + \chi^2_{\text{del}} \tag{5.a}$$

$$\chi^2 = \frac{1}{\sqrt{M-P-1}} \left\{ \sum_{j=1}^{M} \left(\left[\frac{\psi_{\text{exp}}(\omega_j) - \psi_{\text{cal}}(\omega_j)}{\delta\psi(\omega_j)} \right]^2 + \left[\frac{\Delta_{\text{exp}}(\omega_j) - \Delta_{\text{cal}}(\omega_j)}{\delta\Delta(\omega_j)} \right]^2 \right) \right\} \tag{5.b}$$

Table 2
Cauchy Parameters of Al_2O_3 and Glass substrates [48].

Parameter	Al_2O_3	Glass substrate
A	1.559	1.5028
B	0.0052	0.0053
C	0.00004	0.0004

where M and P are the number of data and parameters, respectively; ψ_{exp} and ψ_{cal} are the Ψ from the experiment and calculation, respectively; Δ_{exp} and Δ_{cal} are the Δ from the experiment and calculation at a specific frequency ω_j, respectively; and ($\delta\psi$, $\delta\Delta$) denotes measurement errors in (Ψ, Δ). The Drude-Lorentz equation is given by [46,47,49]:

$$\varepsilon(\omega) = \varepsilon_\infty + \sum_{k=1}^{N} \frac{\omega_{p,k}^2}{\omega_{0,k}^2 - \omega^2 - i\omega\Gamma_k} \tag{6}$$

where ε_∞ shows high-frequency dielectric constants. The parameters $\omega_{p,k}$, $\omega_{0,k}$, and Γ_k declare the plasma frequency, the transverse frequency (eigenfrequency), and the linewidth (scattering rate), respectively, of the *k*-th oscillators. The Bruggeman EMA equation is given by [46,47]:

$$f_a \frac{\varepsilon_a - \varepsilon}{\varepsilon_a + 2\varepsilon} + (1 - f_a) \frac{\varepsilon_b - \varepsilon}{\varepsilon_b + 2\varepsilon} = 0 \tag{7}$$

ε_a and ε_b are the dielectric constant of components *a* and *b*, respectively. f_a and $(1 - f_a)$ indicates the volume fraction of components *a* and *b*, respectively. The real part of optical conductivity (σ_1) is related to the imaginary part of the dielectric constant (ε_2) through the following equation:

$$\sigma_1(\omega) = \frac{\omega\varepsilon_2}{4\pi} \tag{8}$$

The spectral weight (*SW*) measures the effective number of electrons for a particular frequency (or energy) range excited by an incoming photon, and it is given by [50]:

$$SW(\omega_c) = \int_0^{\omega_c} \sigma_1(\omega) d\omega = \frac{\pi n e^2}{2m^*} \tag{9}$$

whereas *n* represents the density of the electron (number of electrons per volume), ω_c is cut-off frequency, and m^* is the effective mass of the electron.

2.3. Density functional theory (DFT) calculation

We performed DFT calculations based on norm-conserving pseudopotentials [51] and optimized pseudoatomic localized basis functions implemented on OpenMX code [52]. The basis function was expanded by a linear combination of multiple pseudoatomic orbitals generated using a confinement scheme [53,54]. In our DFT calculations, we treated the exchange-correlation functional by using generalized-gradient approximation by Perdew, Burke, and Enzerhof (GGA–PBE) [55]. The Bi orbitals were specified by Bi8.0-*s3p2d2f1,* which means that the cutoff radii of the Bi atom is 8.0 Bohr and the calculations included three

s-orbitals, two *p*- and *d*-orbitals, and one *f*-orbitals. The cutoff energy was set to 300 Ry for the charge density. During the structural relaxation, the energy and force convergence criteria are 10^{-8} eV and 5×10^{-3} eV/Å, respectively. We designed a bulk and thin film of Bi crystal model with the lattice parameter $a = b = 4.538$ Å from Ref. [56], as shown in Fig. 2. We added more than 25 Å of vacuum area on the Bi thin film model to appeal to the interactions between two adjacent layers on the *z*-direction. The $8 \times 8 \times 8$ *k*-point grid was used to discretize the First Brillouin Zone (FBZ) for both bulk and thin film Bi models.

3. Results and discussion

Information regarding the structure and morphology is required to establish the quality of the deposited film and to improve the effectiveness of SE measurements in describing the sample. This information supports creating an optical model and using an acceptable dispersion law to determine the dielectric function in the SE process. The AFM images and profiles of Bi films with different thicknesses ($t_{Bi} = 25$ nm, $t_{Bi} = 20$ nm, $t_{Bi} = 15$ nm, and $t_{Bi} = 5$ nm), are shown in Fig. 3 with roughness average (R_a) of 3.05 nm, 3.28 nm, 4.09 nm, and 5.01 nm, respectively.

To show this correlation, we present the structure of selected Bi films ($t_{Bi} = 25$ nm, 20 nm, and 15 nm) investigated by cross-section view SEM, as shown in Fig. 4. Fig. 4(b) depicts a cross-section schematic representation of the structure of the Bi films based on the SEM and AFM data. The film features a discontinuous near-percolation structure at $t_{Bi} = 15$ nm. For $t_{Bi} = 20$ nm and 25 nm, the films exhibit a continuous structure with few voids.

Light scattering occurs when materials contain inhomogeneous characteristics, including porous and patterned structures. When samples depolarize, fully polarised light employed as a probe in ellipsometry is turned into partly polarised light [46]. In some cases, depolarization of incident light affects the measurement seriously, although this effect depends completely on the types of instruments [46]. When samples have a depolarization effect, totally polarized light used as a probe in ellipsometry is transformed into partially polarized light. In this case, the measurement error of the RAE instrument becomes quite large. In the RAE instrument, the polarization state of this reflected light is misinterpreted as elliptical polarization since this instrument assumes totally polarized light for reflected light. This result confirms that the measurement error of RAE increases when the reflected light is partially polarized. In general, when samples have inhomogeneous structures, including porous and patterned structures, light scattering occurs. In our samples, depolarization manifests in ψ data, in which the data is somehow symmetrized around 45° with respect to the model calculation for ψ (in this case, we use a continuous sample surface model). In the RAE configuration, we are using a polarization angle of 45°, which means we have r_p and r_s with the same amplitude; thus, we symmetrized the model around 45° in order to fit ψ data. Meanwhile, we can fit the Δ data quite well using the same model.

Fig. 5 depicts the experimental ψ and Δ of Bi thin films obtained from SE at an incident angle of 70°. A significant increase (decrease) of ψ (Δ) is apparently seen as the thickness of Bi films is decreased, indicating the change of related optical constant. The overall mean squared error (MSE or χ^2) of the fit is 0.08, which is less than 1, indicating a good fitting result.

The complex dielectric constant of Bi thin films extracted by fitting the Drude-Lorentz model to SE data is depicted in Fig. 6. At $t_{Bi} = 5$ nm, the most important are a negative real part (ε_1) values below 2 eV, as shown in Fig. 6(a). The previous studies indicate that the negative ε_1 values in the UV–Vis ranges, and therefore the reported plasmonic properties of Bi nanostructures in this region are generated by the

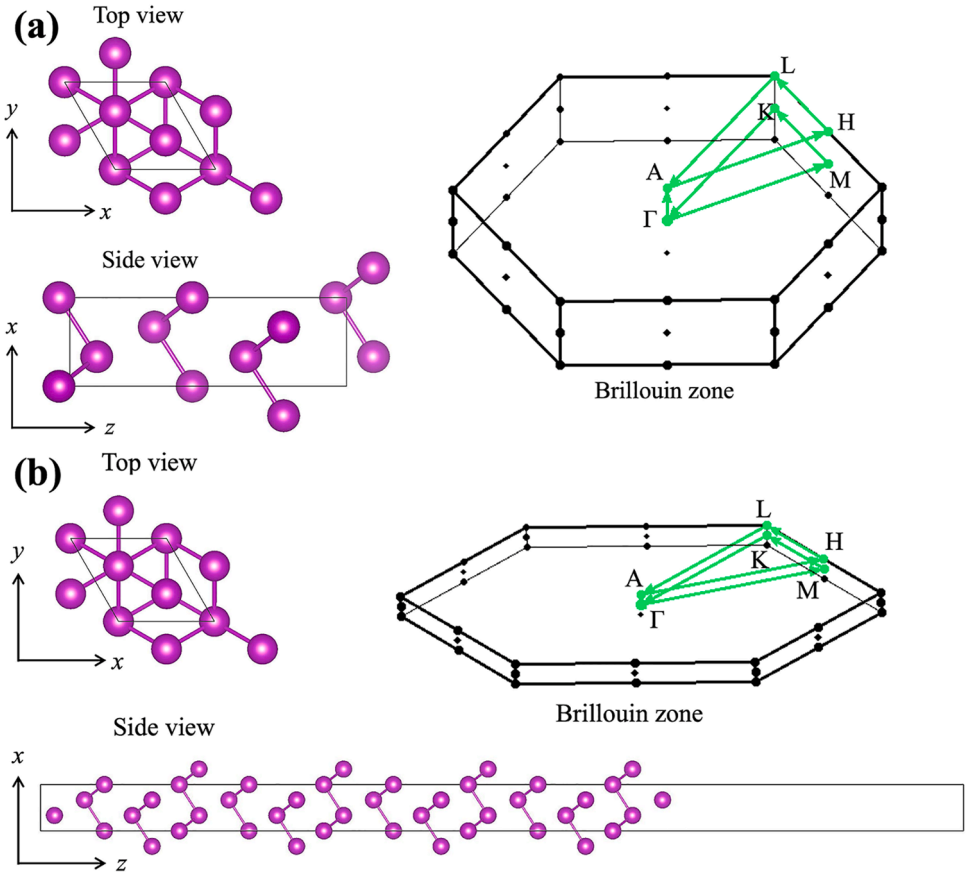

Fig. 2. Bi unit cell and Brillouin zone: **(a)** Bulk Bi and **(b)** 5 nm Bi thin film.

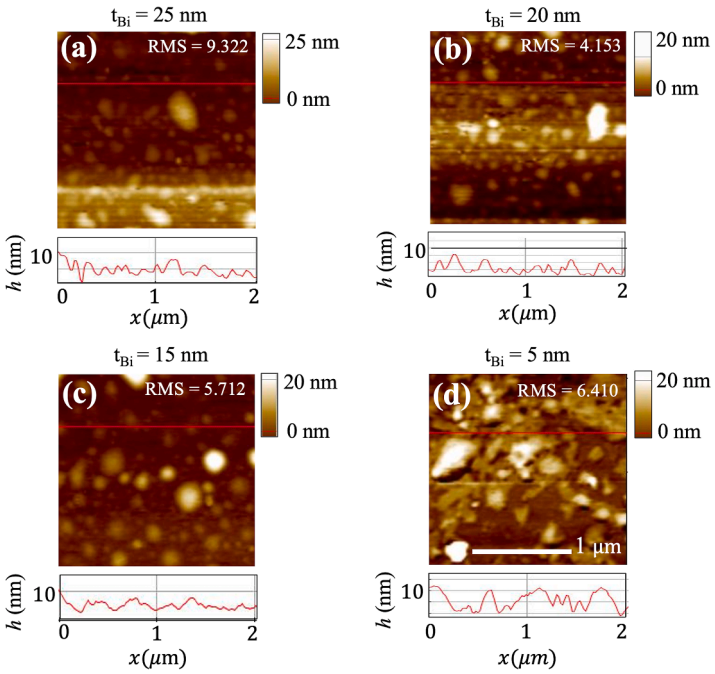

Fig. 3. The AFM images and profiles of Bi films with **(a)** t_{Bi} = 25 nm, **(b)** t_{Bi} = 20 nm, **(b)** t_{Bi} = 15 nm, and **(d)** t_{Bi} = 5 nm.

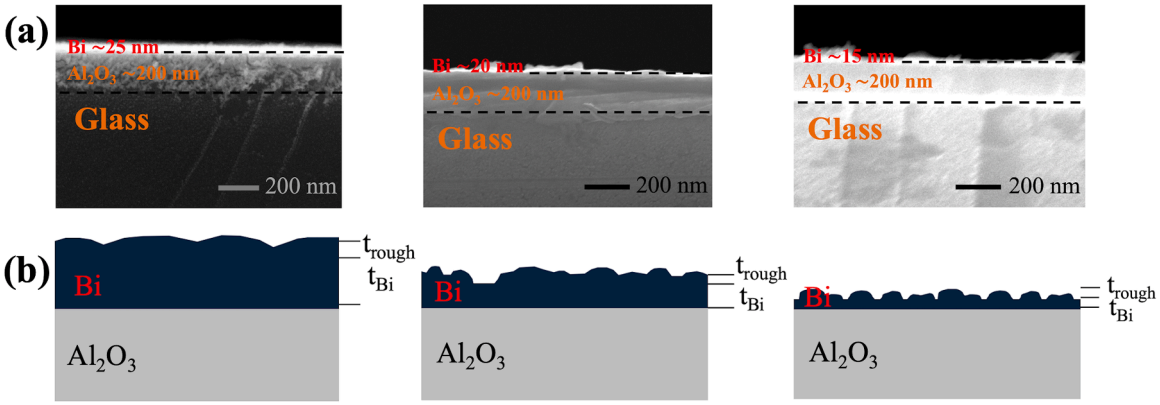

Fig. 4. Structure of selected Bi films (t_{Bi} = 25 nm, t_{Bi} = 20 nm, and t_{Bi} = 15 nm). **(a)** Cross-section view SEM and **(b)** Cross-section schematic representation of the Bi films.

excitation of interband transitions with high oscillator strength [40]. This result refers to a new paradigm in photonics, notably the potential of obtaining interband plasmonic properties in UV–Vis without free carriers [57,58]. Therefore, the optical resonances observed for Bi nanostructures in the UV–Vis regions may be based only on the excitation of interband transitions, with no contribution from free carriers [38,59].

The real part (ε_1) and the imaginary part (ε_2) of the dielectric constant decreases as the thickness change from 25 nm to 15 nm for the spectral range of 1.4 eV to 5.3 eV; however, it increases significantly when the thickness goes to 5 nm for the spectral range of 1.4 eV to 3.5 eV and from 4.1 eV to 5.3 eV. It is apparent that ε_2 is decreases in the range of 3.5 eV to 4.1 eV. In case the thickness of the Bi layer is very thin, the morphology of the layer will not be connected, and the islands will be formed due to the occurrence of inhomogeneity during the growth process, yielding to the formation of the air/void gaps [46].

In Fig. 7(a), the real part of optical conductivity (σ_1), which is related to the absorption of the light (hence the ε_2), shows very distinct features. A broad hump and three broad peaks occur at 2.0 eV and 2.8 eV; 3.8 eV; 5.0 eV, respectively. The origin of these features depends on the dimensionality of the Bi. Toudert et al. argued that the absorption features of Bi films with a thickness varying from 78 nm to 11 nm possess the same absorption features as the bulk Bi in the sense that absorption peak positions do not seem to change. At the same time, their values are decreased as the thickness is reduced [40,6]. It suggests that the electronic structure of the bulk Bi can be employed for the electronic transition assignment as the origin of the related absorption features.

Furthermore, the σ_1 decreases as the thickness change from 25 nm to 15 nm, which might be due to the reduction of the density of states (DOS) of *p*-orbital. In this case, the thickness reduction, hence reducing the volume, will lead to a reduction in the number of electrons involved in the optical transition. Should the thickness reduces further to 5 nm, one may expect that the σ_1 will decrease further; however, it increases significantly. This unexpected result suggests that the DOS of Bi with a thickness of 5 nm increases dramatically; hence the number of electrons per volume per frequency interval is increased. This property can be represented accurately by Fig. 7(b), which depicts the change of the σ_1 (i.e., $\Delta\sigma_1$).

Fig. 7(c) depicts the spectral weight analysis of Bi films in the area that is related to the change of the absorption features (hence the

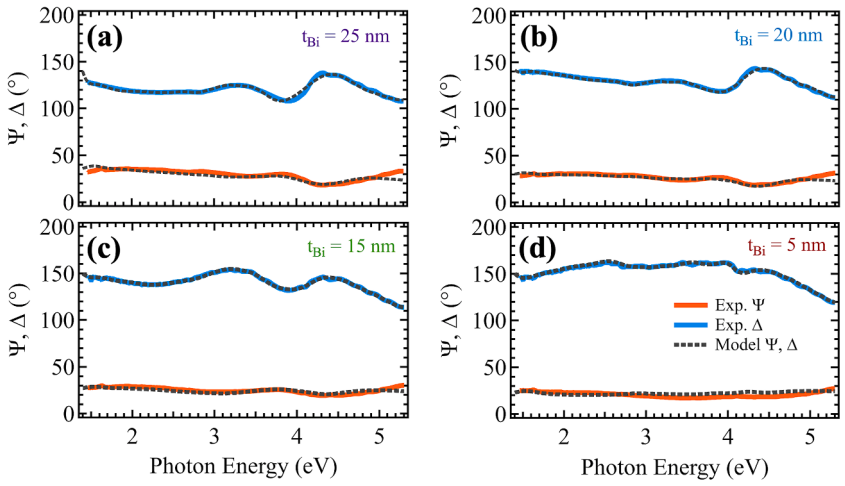

Fig. 5. The ψ and Δ of Bi thin films measured at an incidence angle of 70° with a thickness of **(a)** t_{Bi} = 25 nm, **(b)** t_{Bi} = 20 nm, **(c)** t_{Bi} = 15 nm, and **(d)** t_{Bi} = 5 nm. The solid lines show the experimental results, and the dashed lines show the best match of the fitting result using the optical model in Fig. 1.

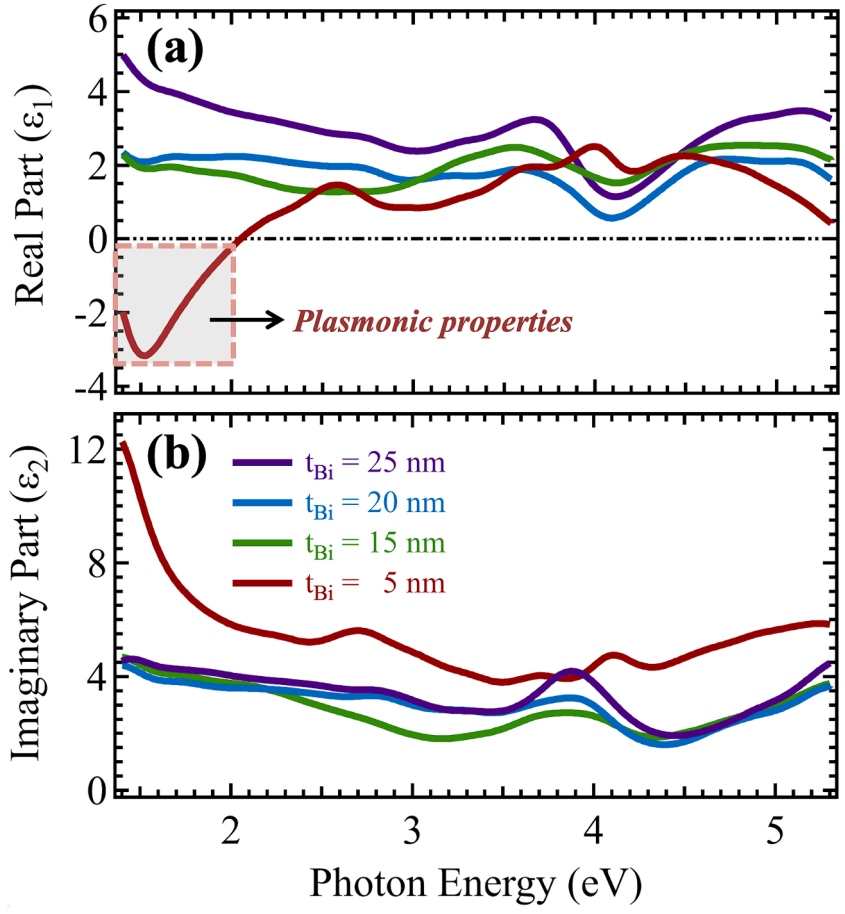

Fig. 6. Complex dielectric constant of Bi films. **(a)** The real part of complex dielectric constants (ε_1) and **(b)** the imaginary part of dielectric constants (ε_2).

number of the electrons) as the thickness is decreased from 25 nm to 5 nm. Area I includes a frequency range from 1.4 eV to 3.5 eV, which covers the absorption hump peaked at 2.0 eV and 2.8 eV, while area II comprises a frequency range from 3.5 eV to 4.5 eV, which covers the absorption peak at 3.8 eV. Area III includes a frequency range from 4.5 eV to 5.3 eV, which covers the absorption peak at 5.0 eV. The spectral weight value in areas I, II, and III decreases with reducing thickness from 25 nm to 15 nm, indicating a carrier downward on the bands associated with the absorption peaks located at that particular range, as described in the previous section. The spectral weight significantly rises at the 5-nm thickness, indicating the addition of the DOS on the band associated with the absorption peaks located at that range (see Fig. 8). Another noticed thing is the possibility of the transition from a three dimension system to two dimensions when the thickness reduces from 15 nm to 5 nm due to the quantum confinement effect. The increase of the DOS at a lower dimension could indicate the quantum confinement effect in our samples, suggesting that the electron movement might be restricted in quasi-two-dimensional space [60]. As the dimension becomes lower, the

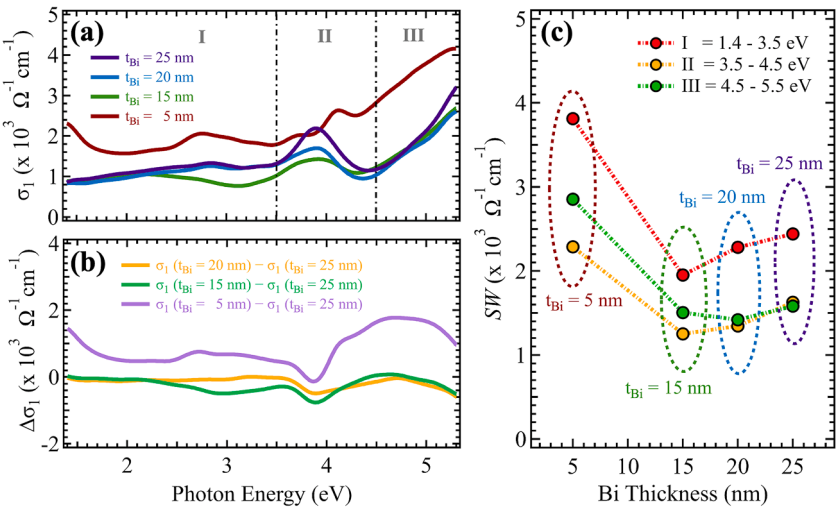

Fig. 7. **(a)** The real part of optical conductivity (σ_1) of Bi films **(b)** The difference in the real part of optical conductivity between Bi with a thickness of 25 nm and that of below 25 nm. **(c)** Spectral weight analysis for three intervals of absorption area of interest. Area I involves an optical range of 1.4 eV – 3.5 eV; area II involves an optical range of 3.5 eV – 4.5 eV; area III involves an optical range of 4.5 eV – 5.3 eV.

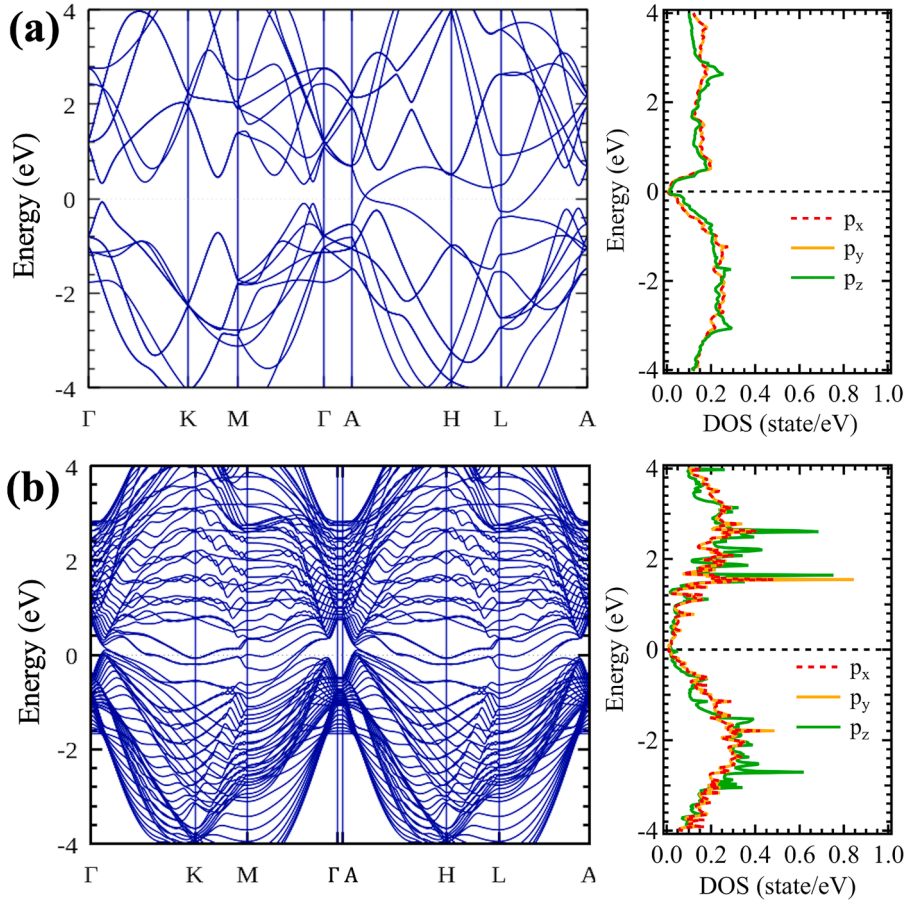

Fig. 8. Band structures (left) and projected density of states, DOS (right) of Bi from density functional theory (DFT) calculations: **(a)** Bulk Bi and **(b)** 5 nm Bi thin film.

surface states of Bi film might contribute to the absorption features in the σ_1. The thermal de Broglie wavelength λ_D ($\lambda_D = h/\sqrt{2\pi m k_B T}$) provides a good approximation of the full-length scale of the quantum confinement effect [61,62]. At room temperature, λ_D is 13.6 nm for semiconductor electrons with a typical effective mass $m^* = 0.1\ m_0$ (m_0: the rest mass of an electron in vacuum), indicating that the crystal diameter is smaller than 13.6 nm.

For a more thorough study, we conducted DFT calculation to examine the obtained optical conductivity data in relation with the band structure of bulk Bi compared with Bi thin film with a thickness of 13 bilayers (~5 nm), as shown in Fig. 8. The conduction (CB) and valence bands (VB) overlapping with an indirect negative band gap is typical of bulk Bi band structures at the Fermi level (see Fig. 8.a). This leads to the formation of small electron and hole pockets on the Fermi surface, which

influence the low-energy electron dynamics of these materials. The electron pocket is at point *L*, whereas the hole pocket is at point *A*. Remarkably, the indirect band gap extends over the whole Brillouin zone. Similar band structure calculation can also be used to describe the electronic transition assignment [25,63], as they provide a similar description of the electronic structure of bulk Bi.

The electronic band structure and DOS of the Bi films with 13 BL thickness are plotted in Fig. 8(b). It is clear that the effect of confinement is most noticeable at *K*, Γ, and *M* points. The states between Γ and M remain relatively close to the Fermi level. We refer to Ref. [1,9,30] for further information. The band structure is dominated by free electron states and an almost flat band, which lies close to the Fermi level. The free electron states have the character of the mixture of the p_x and p_y orbital, while the flat band has the essence of the p_z orbital. All these band formations lead to spikes or singularity in the corresponding DOS contribute to the higher absorption, as compared to bulk Bi.

4. Conclusion

In summary, we have measured spectroscopic ellipsometry on Bi thin films (t_{Bi} = 25 nm, 20 nm, 15 nm, and 5 nm) supported by DFT calculation. We observe a broad absorption hump and three broad absorption peaks, which occur at 2.0 eV and 2.8 eV; 3.8 eV, and 5.0 eV, respectively, for Bi thickness of 25 nm, 20 nm, and 15 nm. These absorption features might be originated from the electronic transitions involving the p_x, p_y orbitals to p_z orbital throughout the high symmetry line of Bi's first Brillouin zone. The absorption peaks decreased as the thickness reduced from 25 nm to 15 nm. However, there is a considerable rise in those absorption peaks at t_{Bi} = 5 nm, which is accompanied by additional absorption peaks at 2.6 eV, 3.0 eV, and 4.1 eV. This anomalous is possibly due to the quantum confinement effect yield to the increase of DOS. Our research may give insight into the future development of Bi-enabled devices.

CRediT authorship contribution statement

Ruth Meisye Kaloari: Conceptualization, Methodology, Investigation, Formal analysis, Writing Original Draft, Visualization.

Eri Widianto: Methodology, Investigation, Formal analysis, Writing Original Draft, Visualization.

I Ketut Agus Putra Dana: Software, Methodology, Investigation.

Arif Lukmantoro: Methodology, DFT Calculation.

Edi Suharyadi: Supervision, Methodology, Investigation.

Takeshi Kato: Methodology, Investigation.

Satoshi Iwata: Methodology, Investigation.

Moh. Adhib Ulil Absor: Methodology, DFT Calculation.

Iman Santoso: Supervision, Funding Acquisition, Interpretation, Review & Editing, Revision, Validation, Submission.

Declaration of Competing Interest

The authors declare that they have no known competing financial interests or personal relationships that could have appeared to influence the work reported in this paper.

Data availability

Data will be made available on request.

Acknowledgments

The authors would like to Faculty of Mathematics and Natural Sciences (FMIPA) University of Gadjah Mada (UGM) and the Ministry of Research, Technology, and Higher Education of the Republic of Indonesia (Kemenristekdikti) to provide partial financial support through Hibah BPPTNBH (No. 130/J01.1.28/PL.06.02/2020) and Hibah WCR (No. 3855/UN1/DITLIT/DIT-LIT/PT/2020). The support from the Nanofabrication Platform Consortium Project of Nagoya University, Ministry of Culture, Sports, Science, and Technology (MEXT) Nano-Project Platform, Japan, is also acknowledged. The authors also would like to thank M. Kumazawa, Nagoya University, for experimental assistance.

References

[1] C. König, J.C. Greer, S. Fahy, Electronic properties of bismuth nanostructures, Phys. Rev. B 104 (2021), 045432, https://doi.org/10.1103/PhysRevB.104.045432.
[2] A.K. Kundu, G. Gu, T. Valla, Quantum size effects, multiple dirac cones, and edge states in ultrathin Bi(110) films, ACS. Appl. Mater. Interfaces 13 (2021) 33627–33634, https://doi.org/10.1021/acsami.1c06821.
[3] Y. Li, J. Zhang, X. Xu, W. Hao, J. Zhuang, Y. Du, Advances in bismuth-based topological quantum materials by scanning tunnelling microscopy, Mater. Futures (2022), https://doi.org/10.1088/2752-5724/ac84f5.
[4] J. Wang, X. Sun, H. Du, C. Ma, B. Wang, Electronic and topological properties of Bi (110) ultrathin films grown on a Cu(111) substrate, Phys. Rev. B 105 (2022), 115407, https://doi.org/10.1103/PhysRevB.105.115407.
[5] B. He, G. Tian, J. Gou, B. Liu, K. Shen, Q. Tian, Z. Yu, F. Song, H. Xie, Y. Gao, Y. Lu, K. Wu, L. Chen, H. Huang, Structural and electronic properties of atomically thin Bismuth on Au (111), Surf. Sci. 679 (2019) 147–153, https://doi.org/10.1016/j.susc.2018.09.005.
[6] J. Toudert, R. Serna, C. Deeb, E. Rebollar, Optical properties of bismuth nanostructures towards the ultrathin film regime, Opt. Mater. Express 9 (2019) 2924, https://doi.org/10.1364/OME.9.002924.
[7] H. Du, X. Sun, X. Liu, X. Wu, J. Wang, M. Tian, A. Zhao, Y. Luo, J. Yang, B. Wang, J. G. Hou, Surface Landau levels and spin states in bismuth (111) ultrathin films, Nat. Commun 7 (2016) 10814, https://doi.org/10.1038/ncomms10814.
[8] P. Di Pietro, F.M. Vitucci, D. Nicoletti, L. Baldassarre, P. Calvani, R. Cava, Y.S. Hor, U. Schade, S. Lupi, Optical conductivity of bismuth-based topological insulators, Phys. Rev. B 86 (2012), 045439, https://doi.org/10.1103/PhysRevB.86.045439.
[9] Y.M. Koroteev, G. Bihlmayer, E.v. Chulkov, S. Blügel, First-principles investigation of structural and electronic properties of ultrathin Bi films, Phys. Rev. B 77 (2008), 045428, https://doi.org/10.1103/PhysRevB.77.045428.
[10] T. Hirahara, The Rashba and quantum size effects in ultrathin Bi films, J. Electron. Spectros. Relat. Phenomena 201 (2015) 98–104, https://doi.org/10.1016/j.elspec.2014.08.004.
[11] T. Hirahara, G. Bihlmayer, Y. Sakamoto, M. Yamada, H. Miyazaki, S. Kimura, S. Blügel, S. Hasegawa, Interfacing 2D and 3D topological insulators: bi(111) bilayer on Bi_2Te_3, Phys. Rev. Lett 107 (2011), 166801, https://doi.org/10.1103/PhysRevLett.107.166801.
[12] S. Ito, B. Feng, M. Arita, A. Takayama, R.-.Y. Liu, T. Someya, W.-.C. Chen, T. Iimori, H. Namatame, M. Taniguchi, C.-.M. Cheng, S.-.J. Tang, F. Komori, K. Kobayashi, T.-.C. Chiang, I. Matsuda, Proving nontrivial topology of pure bismuth by quantum confinement, Phys. Rev. Lett 117 (2016), 236402, https://doi.org/10.1103/PhysRevLett.117.236402.
[13] E.I. Rogacheva, S.G. Lyubchenko, M.S. Dresselhaus, Semimetal–semiconductor transition in thin Bi films, Thin. Solid. Films 516 (2008) 3411–3415, https://doi.org/10.1016/j.tsf.2007.11.023.
[14] C.A. Hoffman, J.R. Meyer, F.J. Bartoli, A. Di Venere, X.J. Yi, C.L. Hou, H.C. Wang, J.B. Ketterson, G.K. Wong, Semimetal-to-semiconductor transition in bismuth thin films, Phys. Rev. B 51 (1995) 5535–5537, https://doi.org/10.1103/PhysRevB.51.5535.
[15] S. He, A. Bahrami, X. Zhang, I.G. Martínez, S. Lehmann, K. Nielsch, Effect of powder ALD interface modification on the thermoelectric performance of Bismuth, Adv. Mater. Technol 7 (2022), 2100953, https://doi.org/10.1002/admt.202100953.
[16] C. Redondo-Obispo, I. Suárez, S.J. Quesada, T.S. Ripolles, J.P. Martínez-Pastor, A. L. Álvarez, A. de Andrés, C. Coya, Enhanced nonlinear optical coefficients of $MAPbI_3$ thin films by Bismuth doping, J. Phys. Chem. Lett 11 (2020) 2188–2194, https://doi.org/10.1021/acs.jpclett.0c00319.
[17] B. Weitzel, H. Micklitz, Superconductivity in granular systems built from well-defined rhombohedral Bi-clusters: evidence for Bi-surface superconductivity, Phys. Rev. Lett 66 (1991) 385–388, https://doi.org/10.1103/PhysRevLett.66.385.
[18] J. Xiong, P. Song, J. Di, H. Li, Z. Liu, Freestanding ultrathin bismuth-based materials for diversified photocatalytic applications, J. Mater. Chem. A. Mater 7 (2019) 25203–25226, https://doi.org/10.1039/C9TA10144F.
[19] T. Chen, F. Meng, Z. Zhang, J. Liang, Y. Hu, W. Kong, X.L. Zhang, Z. Jin, Stabilizing lithium metal anode by molecular beam epitaxy grown uniform and ultrathin bismuth film, Nano. Energy 76 (2020), 105068, https://doi.org/10.1016/j.nanoen.2020.105068.
[20] Z. He, Y. Gong, Z. Tan, Recent advances in Bismuth-based solar cells: fundamentals, fabrication, and optimization strategies, Adv. Sustain. Syst 6 (2022), 2200051, https://doi.org/10.1002/adsu.202200051.
[21] O. Prakash, A. Kumar, A. Thamizhavel, S. Ramakrishnan, Evidence for bulk superconductivity in pure bismuth single crystals at ambient pressure, Science 355 (2017) 52–55, https://doi.org/10.1126/science.aaf8227 (1979).
[22] L. Wang, L. Wang, Y. Du, X. Xu, S.X. Dou, Progress and perspectives of bismuth oxyhalides in catalytic applications, Mater. Today. Phys 16 (2021), https://doi.org/10.1016/j.mtphys.2020.100294.

[23] M.A. Ud Din, C. Li, L. Zhang, C. Han, B. Li, Recent progress and challenges on the bismuth-based anode for sodium-ion batteries and potassium-ion batteries, Mater. Today Physics 21 (2021), https://doi.org/10.1016/j.mtphys.2021.100486.
[24] I. Aguilera, C. Friedrich, S. Blügel, Electronic phase transitions of bismuth under strain from relativistic self-consistent *GW* calculations, Phys. Rev. B 91 (2015), 125129, https://doi.org/10.1103/PhysRevB.91.125129.
[25] P. Hofmann, The surfaces of bismuth: structural and electronic properties, Prog. Surf. Sci 81 (2006) 191–245, https://doi.org/10.1016/j.progsurf.2006.03.001.
[26] X. Gonze, J.-P. Michenaud, J.-P. Vigneron, First-principles study of As, Sb, and Bi electronic properties, Phys. Rev. B 41 (1990) 11827–11836, https://doi.org/10.1103/PhysRevB.41.11827.
[27] S. Murakami, Quantum spin hall effect and enhanced magnetic response by spin-orbit coupling, Phys. Rev. Lett 97 (2006), 236805, https://doi.org/10.1103/PhysRevLett.97.236805.
[28] J.-P. Issi, Low Temperature transport properties of the Group V semimetals, Austral. J. Phys 32 (1979) 585, https://doi.org/10.1071/PH790585.
[29] Y. Lu, W. Xu, M. Zeng, G. Yao, L. Shen, M. Yang, Z. Luo, F. Pan, K. Wu, T. Das, P. He, J. Jiang, J. Martin, Y.P. Feng, H. Lin, X. Wang, Topological properties determined by atomic buckling in self-assembled ultrathin Bi(110), Nano. Lett. 15 (2015) 80–87, https://doi.org/10.1021/nl502997v.
[30] H. Ishida, Decay length of surface-state wave functions on Bi (111), Journal. of. Phys 29 (2017), 015002, https://doi.org/10.1088/0953-8984/29/1/015002.
[31] M.Z. Hasan, C.L. Kane, Colloquium : topological insulators, Rev. Mod. Phys 82 (2010) 3045–3067, https://doi.org/10.1103/RevModPhys.82.3045.
[32] C. Zucchetti, M.-T. Dau, F. Bottegoni, C. Vergnaud, T. Guillet, A. Marty, C. Beigné, S. Gambarelli, A. Picone, A. Calloni, G. Bussetti, A. Brambilla, L. Duò, F. Ciccacci, P.K. Das, J. Fujii, I. Vobornik, M. Finazzi, M. Jamet, Tuning spin-charge interconversion with quantum confinement in ultrathin bismuth films, Phys. Rev. B 98 (2018), 184418, https://doi.org/10.1103/PhysRevB.98.184418.
[33] X. Li, H. Liu, H. Jiang, F. Wang, J. Feng, Edge engineering of a topological Bi (111) bilayer, Phys. Rev. B 90 (2014), 165412, https://doi.org/10.1103/PhysRevB.90.165412.
[34] L. Yang, Y.-X. Zheng, S.-D. Yang, Z.-H. Liu, J.-B. Zhang, R.-J. Zhang, S.-Y. Wang, D.-X. Zhang, L.-Y. Chen, Ellipsometric study on temperature dependent optical properties of topological bismuth film, Appl. Surf. Sci 421 (2017) 899–904, https://doi.org/10.1016/j.apsusc.2016.11.006.
[35] D.-H. Kim, S.-H. Lee, J.-K. Kim, G.-H. Lee, Structure and electrical transport properties of bismuth thin films prepared by RF magnetron sputtering, Appl. Surf. Sci 252 (2006) 3525–3531, https://doi.org/10.1016/j.apsusc.2005.05.046.
[36] L. Meng, W. Xu, Q. Zhang, T. Yang, S. Shi, Study of nanostructural bismuth oxide films prepared by radio frequency reactive magnetron sputtering, Appl. Surf. Sci 472 (2019) 165–171, https://doi.org/10.1016/j.apsusc.2018.02.017.
[37] E. Rodríguez-Schwendtner, A. Álvarez-Herrero, A. Mariscal, R. Serna, A. González-Cano, M.-C. Navarrete, N. Díaz-Herrera, Ellipsometric characterization of Bi and Al_2O_3 coatings for plasmon excitation in an optical fiber sensor, J. Vacuum Sci. Technol. B 37 (2019), 062914, https://doi.org/10.1116/1.5121590.
[38] J. Toudert, R. Serna, M. Jiménez de Castro, Exploring the optical potential of nano-bismuth: tunable surface plasmon resonances in the near ultraviolet-to-near infrared range, J. Phys. Chem. C 116 (2012) 20530–20539, https://doi.org/10.1021/jp3065882.
[39] R. Tediosi, N.P. Armitage, E. Giannini, D. van der Marel, Charge carrier interaction with a purely electronic collective mode: plasmarons and the Infrared response of elemental Bismuth, Phys. Rev. Lett 99 (2007), 016406, https://doi.org/10.1103/PhysRevLett.99.016406.
[40] J. Toudert, R. Serna, I. Camps, J. Wojcik, P. Mascher, E. Rebollar, T.A. Ezquerra, Unveiling the far infrared-to-ultraviolet optical properties of Bismuth for applications in plasmonics and nanophotonics, J. Phys. Chem. C 121 (2017) 3511–3521, https://doi.org/10.1021/acs.jpcc.6b10331.
[41] J. Bulíř, J. More-Chevalier, S. Chertopalov, L. Fekete, L. Volfová, P. Hubík, M. Novotný, J. Lančok, Analysis of thickness-dependent electron transport in magnetron sputtered ZrN films by spectroscopic ellipsometry, Thin. Solid. Films 731 (2021), https://doi.org/10.1016/j.tsf.2021.138746.
[42] R.S. Gonçalves, P. Barrozo, G.L. Brito, B.C. Viana, F. Cunha, The effect of thickness on optical, structural and growth mechanism of ZnO thin film prepared by magnetron sputtering, Thin. Solid. Films 661 (2018) 40–45, https://doi.org/10.1016/j.tsf.2018.07.008.
[43] A. Herawati, R.A.N. Khasanah, L.Z. Maulana, E. Suharyadi, I. Santoso, Simple and low-cost rotating analyzer ellipsometer (RAE) for wavelength dependent optical constant characterization of novel materials, Key. Eng. Mater 840 (2020) 392–398, https://doi.org/10.4028/www.scientific.net/KEM.840.392.
[44] I.K. Agus Putra Dana, P.D. Jatmiko, E. Suharyadi, I. Santoso, A compact, modular, multi-wavelength (200-850 nm) rotating-analyzer ellipsometer for optical constant characterization of nanostructured materials, Eur. J. Phys 41 (2020) 65303, https://doi.org/10.1088/1361-6404/ab9b3e.
[45] R.M. Kaloari, Study of Thickness Effect On Optical Properties of Bismuth ultrathin Film Using Ellipsometry Spectroscopy At Wavelength 220 Nm - 850 nm, Universitas Gadjah Mada, 2020. Magister Thesis.
[46] H. Fujiwara, Spectroscopic Ellipsometry: Principles and Applications, John Wiley & Sons, Ltd, UK, 2007.
[47] H. Fujiwara, R.W. Collins, Spectroscopic ellipsometry for photovoltaics volume 1: fundamental principles and solar cell characterization, 2018. 10.1007/978-3-319-75377-5.
[48] G. de la Rosa-Santana, J.A. Alvarez-Chavez, H.R. Morano-Okuno, A.J. Morales-Ramirez, E. Uribe, Photomechanical ablation of 304 L stainless steel, aluminum oxide (Al2O3) thin film, and pure silicon, Optics Photon. J 06 (2016) 275–288, https://doi.org/10.4236/opj.2016.610028.
[49] A.B. Kuzmenko, Kramers-Kronig constrained variational analysis of optical spectra, Rev. Scient. Instrum 76 (2005) 1–9, https://doi.org/10.1063/1.1979470.
[50] T.J. Whitcher, A.D. Fauzi, D. Caozheng, X. Chi, A. Syahroni, T.C. Asmara, M.B. H. Breese, A.H.C. Neto, A.T.S. Wee, M.A. Majidi, A. Rusydi, Unravelling strong electronic interlayer and intralayer correlations in a transition metal dichalcogenide, Nat. Commun 12 (2021) 1–10, https://doi.org/10.1038/s41467-021-27182-y.
[51] N. Troullier, J.L. Martins, Efficient pseudopotentials for plane-wave calculations, Phys. Rev. B 43 (1991), https://doi.org/10.1103/PhysRevB.43.1993.
[52] T. Ozaki, H. Kino, J. Yu, M.J. Han, N. Kobayashi, M. Ohfuti, F. Ishii, T. Ohwaki, H. Weng, K. Terakura, OpenMX, (2009). http://www.openmx-square.org/.
[53] T. Ozaki, Variationally optimized atomic orbitals for large-scale electronic structures, Phys. Rev. B. 67 (2003), 155108, https://doi.org/10.1103/PhysRevB.67.155108.
[54] T. Ozaki, H. Kino, Numerical atomic basis orbitals from H to Kr, Phys. Rev. B. 69 (2004), 195113, https://doi.org/10.1103/PhysRevB.69.195113.
[55] J.P. Perdew, K. Burke, M. Ernzerhof, Generalized gradient approximation made simple, Phys. Rev. Lett. 77 (1996) 3865–3868, https://doi.org/10.1103/PhysRevLett.77.3865.
[56] H. Kotaka, F. Ishii, M. Saito, First-principles study of spin texture and Fermi lines in Bi (111) multi-layer nanofilm, ArXiv:. Mater. Sci (2017), https://doi.org/10.48550/arXiv.1703.08287.
[57] J. Toudert, R. Serna, Ultraviolet-visible interband plasmonics with p-block elements, Opt. Mater. Express 6 (2016) 2434, https://doi.org/10.1364/OME.6.002434.
[58] J.-Y. Ou, J.-K. So, G. Adamo, A. Sulaev, L. Wang, N.I. Zheludev, Ultraviolet and visible range plasmonics in the topological insulator $Bi_{1.5}Sb_{0.5}Te_{1.8}Se_{1.2}$, Nat. Commun 5 (2014) 5139, https://doi.org/10.1038/ncomms6139.
[59] A. Cuadrado, J. Toudert, R. Serna, Polaritonic-to-plasmonic transition in optically resonant bismuth nanospheres for high-contrast switchable ultraviolet meta-filters, IEEE. Photon. J 8 (2016) 1–11, https://doi.org/10.1109/JPHOT.2016.2574777.
[60] D. Natelson, Nanostructures and Nanotechnology, Cambridge University Press, 2015, https://doi.org/10.1017/CBO9781139025485.
[61] Kittel Charles, Introduction to Solid State Physics, 8th ed., John Wiley & Sons, Inc, New York, 2005.
[62] N.T. Hung, A.R.T. Nugraha, T. Yang, R. Saito, Confinement effect in thermoelectric properties of two–dimensional materials, MRS. Adv 5 (2020) 469–479, https://doi.org/10.1557/adv.2020.128.
[63] G. Bian, X. Wang, P.J. Kowalczyk, T. Maerkl, S.A. Brown, T.-C. Chiang, Survey of electronic structure of Bi and Sb thin films by first-principles calculations and photoemission measurements, J. Phys. Chem. Solids 128 (2019) 109–117, https://doi.org/10.1016/j.jpcs.2017.07.027.